Automatic detection and segmentation of renal lesions in 3D contrast-enhanced ultrasound images

Raphaël Prevost, Laurent D. Cohen, Jean-Michel Corréas, Roberto Ardon

Automatic detection and segmentation of renal lesions in 3D contrast-enhanced ultrasound images

Raphael Prevost[a,b], Laurent D. Cohen[b], Jean-Michel Correas[c], Roberto Ardon[a]

[a] Medisys Research Lab, Philips Healthcare, Suresnes, France.
[b] CEREMADE, UMR 7534 CNRS, Paris Dauphine University, Paris, France.
[c] Department of Adult Radiology, Hopital Necker, Paris, France.

ABSTRACT

Contrast-enhanced ultrasound (CEUS) is a valuable imaging modality in the detection and evaluation of different kinds of lesions. Three-dimensional CEUS acquisitions allow quantitative volumetric assessments and better visualization of lesions, but automatic and robust analysis of such images is very challenging because of their poor quality. In this paper, we propose a method to automatically segment lesions such as cysts in 3D CEUS data. First we use a pre-processing step, based on the guided filtering framework, to improve the visibility of the lesions. The lesion detection is then performed through a multi-scale radial symmetry transform. We compute the likelihood of a pixel to be the center of a dark rounded shape. The local maxima of this likelihood are considered as lesions centers. Finally, we recover the whole lesions volume with multiple front propagation based on image intensity, using a fast marching method. For each lesion, the final segmentation is chosen as the one which maximizes the gradient flux through its boundary. Our method has been tested on several clinical 3D CEUS images of the kidney and provides promising results.

Keywords: contrast-enhanced, 3D, ultrasound, detection, segmentation, filtering, kidney, lesions, cysts, front propagation, fast marching

1. INTRODUCTION

Three-dimensional (3D) real-time monitoring of vascularization can be achieved with contrast-enhanced ultrasound (CEUS) imaging. Gas-filled microbubbles, acting as amplifiers of the blood backscattering signal, are used as a contrast agent. They typically last a few minutes in the circulation before being taken up by immune system cells. Their gas is then expired through the lungs whereas their membrane is eliminated by some metabolism processes. This modality is therefore considered as completely safe for the patients even with renal or liver failure [1]. Recent studies showed that CEUS can be very useful for lesions diagnosis, and may even compete with CT or MR [2].

Manual assessment of 3D lesions characteristics is currently very tedious, especially when the lesions are numerous. An automatic tool of lesions detection and segmentation would be time-saving and thus very useful for the clinicians. Moreover, it could also be used as an intermediate step to perform intra-patient image registration. Indeed, lesions represent anatomical landmarks that could drive a feature-based registration algorithm.

However, although a few attempts were made to design interactive segmentation algorithms [3] [4], no automatic solution has yet been proposed to the authors knowledge. The nature of CEUS images makes this task very challenging: in addition to having powerful speckle noise, the image is very grainy as a result of ultrasound interactions with the contrast agent (composed of quite large bubbles).

In this paper, we present a fully automatic method to detect and segment lesions in the kidney. We will here exclusively focus on anechogenic rounded masses, such as cysts, tumour necrosis or burnt tumours (after radio-frequency ablation).

In Section 2, we describe the acquisition conditions of the images that we are working on, and propose a fast pre-processing step based on guided filtering [5]. Section 3 then describes our adaptation of the fast radial symmetry transform [6] to detect potential lesions centers. Segmentation is finally achieved with multiple front propagation (presented in Section 4), initialized from the detected centers. We show some results and discuss potential applications and improvements in Section 5.

2. IMAGE MATERIAL AND PRE-PROCESSING

2.1 Image acquisition

In this study, we work on 3D images acquired from a iU22 ultrasound system (Philips, The Netherlands). Two different probes (V6-2 and X6-1) were used, with various spatial resolutions and fields of view. The patients were injected with 2.4 mL of SonoVue contrast agent (Bracco, Italy).

Dynamic CEUS images of a kidney show a cortical enhancement shortly followed by a medullary enhancement. Our working images (see Figure 1) are acquired a few seconds after the contrast agent injection. Better visualization of kidney tissue is then available as it is completely hyperechoic whereas its fatty surrounding and lesions of interest produce no signal.

2.2 Region of interest

The lesion detection and segmentation will be limited inside a mask M_K delineating the kidney (1 inside and 0 outside). The kidney segmentation is automatic but out of the scope of this paper.

2.3 Pre-processing with guided filtering

Lesion detection is highly influenced by speckle and granular noise. In order to reduce it without smoothing out weak image structures and preserve edges, we apply a fast anisotropic filter. We use the *guided filtering* framework recently introduced in [5]. Denoting the original image I, the filtered image $\tilde{I}$ is defined as a locally affine transform of I. For each window W_x centered in the pixel x,

$$\forall y \in W_x \ , \quad \tilde{I}(y) = a_x I(y) + b_x \tag{1}$$

where a_x and b_x are constant coefficients in W_x. They are chosen in order to minimize on one hand the difference between I and $\tilde{I}$ and, on the other hand, the magnitude of a_x :

$$a_x, b_x = \underset{a,b}{\operatorname{argmin}} \left\{ E_x(a,b) = \sum_{y \in W_x} (aI(y) + b - I(y))^2 + \lambda^2 a^2 \right\} \tag{2}$$

The solution of Problem (2) can be directly computed by solving $\dfrac{\partial E_x}{\partial a}(a_x, b_x) = \dfrac{\partial E_x}{\partial b}(a_x, b_x) = 0$:

$$a_x = \frac{\sigma_x^2}{\sigma_x^2 + \lambda^2} \qquad\qquad b_x = (1 - a_x)\ \mu_x \tag{3}$$

where μ_x and σ_x^2 are the mean and variance of I in W_x. The coefficients a_x and b_x can thus be computed for all windows W_x. However, because the windows are overlapping, $\tilde{I}(x)$ has different values for each window that includes x. The filtered image is then rather defined as the mean of these values computed for all involved windows :

$$\begin{aligned} \tilde{I}(y) &= \frac{1}{|W_x|} \sum_{x | y \in W_x} a_x I(y) + b_x \\ &= \left(\frac{1}{|W_x|} \sum_{x | y \in W_x} a_x \right) I(y) + \left(\frac{1}{|W_x|} \sum_{x | y \in W_x} b_x \right) \end{aligned} \tag{4}$$

From Eq. (3), we point out that in areas where I has a small variance, $a \approx 0$ and $b \approx \mu_x$ so the guided filter has the same behaviour than a mean filter. Conversely, near edges, σ_x^2 is high so $a \approx 1$ and $b \approx 0$, which means that the image is not changed. Both the parameter λ and the size of the windows control the smoothness of the filtered image.

This filtering has a time-complexity depending on the kind of windows W_x, but generally in $O(n)$. The most common choice for W_x are cuboids, in which case the window indicator is a kernel $K_W^\sigma(z) = 1_{\{\|z\|_\infty \leq \sigma\}}$. But the window indicator K_W^σ can also be chosen as a fuzzy kernel, for example Gaussian. It can be performed very efficiently, using integral images (if W_x are cuboids) or fast recursive implementations. Results of the pre-processing on two different 3D CEUS images are shown on Figure 1. This illustrates the smoothing but edge-preserving properties of the filtering.

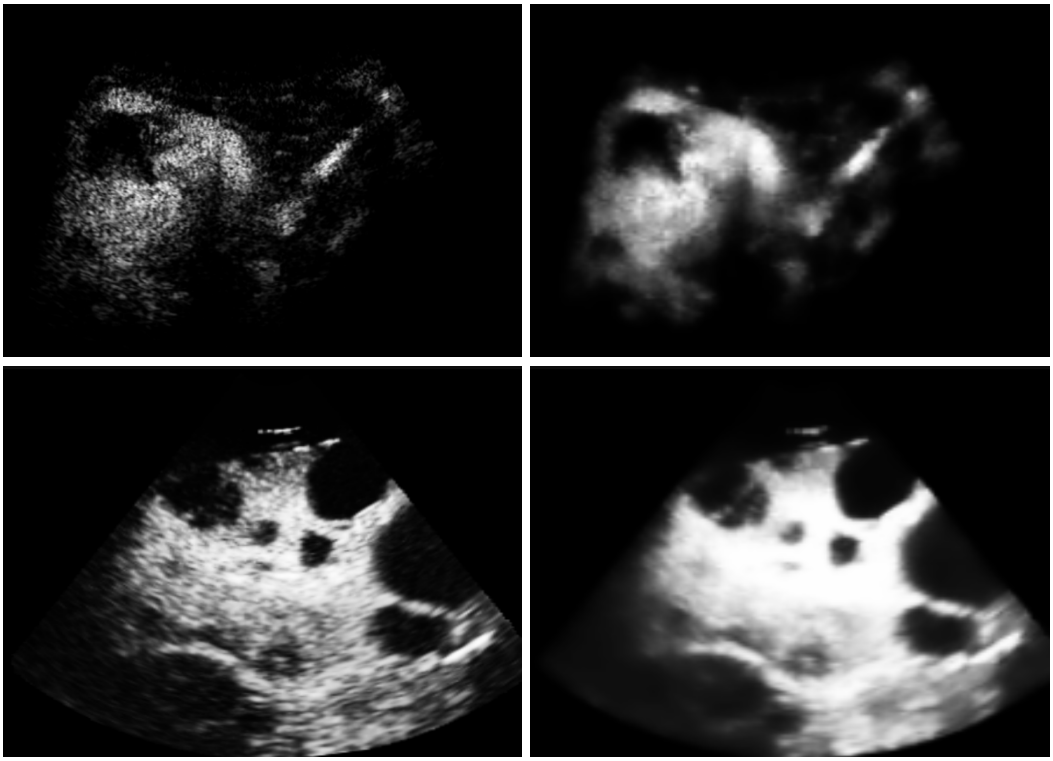

Figure 1. Slices of two 3D CEUS images of a kidney (with one or several lesions before (left) and after (right) the guided filtering.

3. LESION DETECTION

Lesions detection is performed by searching for dark spherical shapes in the filtered image. Shape detection can be achieved with Hough transforms (e.g. [7]), but these methods generally either are time-consuming in 3D (in the case of ellipsoid detection) or lack robustness (in the case of sphere detection). Blobs can also be detected with a multi-scale analysis of the Hessian matrix [8], but this technique is unable to distinguish large objects separated by small structures. Conversely, the Fast Radial Symmetry Transform, detailed hereafter, does not suffer from such problems.

3.1 Fast Radial Symmetry Transform

The Fast Radial Symmetry Transform (FRST) was originally described in [6] to detect points of interest in 2D images. We adapted this method to find centers of large dark rounded shapes in 3D images. To detect blobs of radius r, we browse the image and associate to every voxel p the point $\tilde{p}_r = p - r\frac{\nabla I(p)}{\|\nabla I(p)\|}$ and "vote" for it in two different accumulators :

$$O_r(\tilde{p}_r) \leftarrow O_r(\tilde{p}_r) + 1 \tag{5}$$

$$M_r(\tilde{p}_r) \leftarrow M_r(\tilde{p}_r) + \|\nabla I(p)\| \tag{6}$$

The first accumulator $O_r(x)$ counts the number of pixels at distance r that voted for x, while the second takes also into account the magnitude of the gradient to weigh each contribution. As shown in Figure 2a and 2b, a point at the center of a circle of radius r will receive contributions from the whole boundary and therefore have a high value of O_r and M_r. The symmetry transform for a given radius r is defined as

$$S_r(x) = \left[M_r \left(\frac{O_r}{\max\limits_{y \in \Omega} O_r(y)} \right)^{\alpha} \right] * K_{\sigma(r)}(x) \tag{7}$$

where α is a parameter defining the strictness to radial symmetry and $K_{\sigma(r)}$ is a 3D Gaussian kernel. The purpose of this convolution is on the one hand to spread the votes in neighbouring voxels (to improve robustness), and on the other hand to normalize the terms of different scales. Indeed, we set its standard deviation as a function of the current radius : $\sigma(r) = \frac{r}{2}$.

The contributions of the N_r different radii are finally averaged to define the final FRST criterion :

$$S(x) = \frac{1}{N_r} \sum_{r=r_{min}}^{r_{max}} \left[M_r \left(\frac{O_r}{\max\limits_{y \in \Omega} O_r(y)} \right)^{\alpha} \right] * K_{\sigma(r)}(x) \tag{8}$$

The computation complexity of the FRST is $O(n\ N_r)$. Figure 2c illustrates S on a 2D synthetic image, whereas Figure 3 shows it for real 3D CEUS data. One can notice that the response is indeed stronger at centers of dark blobs.

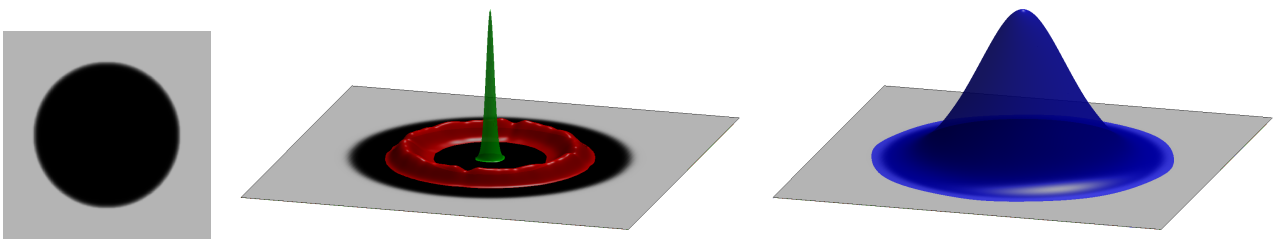

(a) (b) (c)

Figure 2. Computation of the Fast Radial Symmetry Transform on a synthetic 2D image of a dark circle (a). (b) Accumulator O for two different radii. For the correct radius, the whole circle boundary will contribute to the same point (green surface), whereas the contributions will be diluted in other points if the radius is incorrect (red surface). (b) Final criterion S (blue surface) for a range of different radii.

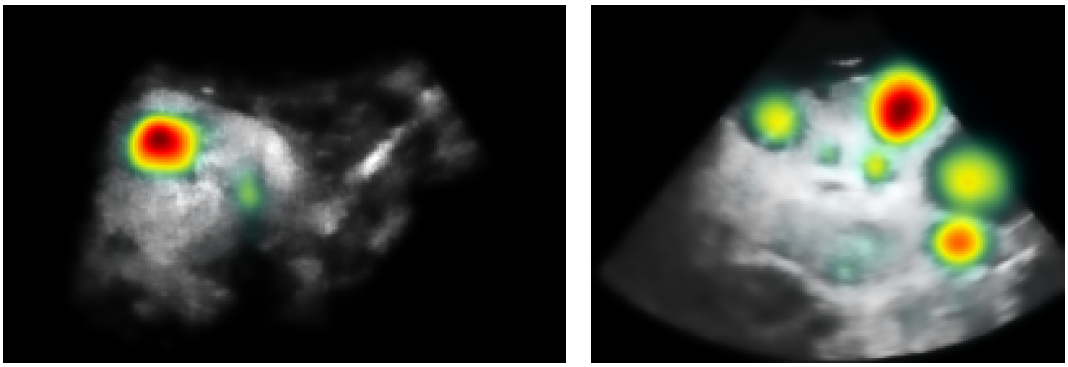

(a) (b)

Figure 3. Response of the FRST inside the kidney superimposed on the CEUS images presented in Figure 1, with $\alpha = 2$, $r \in [5\text{ mm}, 20\text{ mm}]$. Red (resp. green) indicates high (resp. low) values. Note that these are slices of a 3D response: the cyst at the right side of image (b) seems to respond weakly but actually the slice does not correspond to its 3D center.

3.2 Extraction of lesions centers

We consider as potential centers of lesions all local maxima of S above a given threshold. However, some lesions are more ellipsoidal than spherical. When their shape is too anisotropic, the maximum at the center may split into two local maxima, as demonstrated in Figure 4. To avoid such problems, we sift the set of centers by applying the following rule : for each pair of potential centers (x_i, x_j), we compute the quantity

$$m(x_i, x_j) = \max_{t \in [0;1]} \tilde{I}(t\ x_i + (1-t)\ x_j) \tag{9}$$

which represents the maximum intensity of the image along the path between x_i and x_j. Assuming each lesion is convex, $m(x_i, x_j)$ will be low (below a fixed threshold) if and only if x_i and x_j belong to the same lesion. In this case, we merge them into a new center. This step guarantees a one-to-one correspondance between detected centers and lesions.

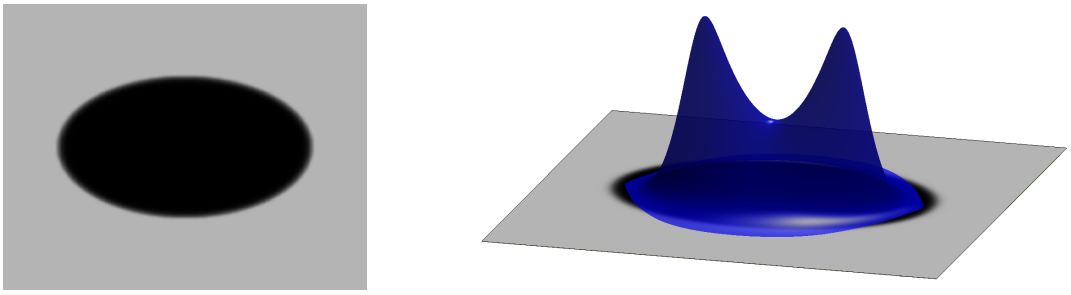

(a) (b)

Figure 4. (a) Synthetic 2D image of a dark ellipse. (b) Computation of the Fast Radial Symmetry Transform S (blue surface) show that two different local maxima can appear if the shape deviates too much from a disk.

4. LESION SEGMENTATION

At this stage, lesions centers have been detected. We now recover the whole lesions from these centers, with a front propagation approach, which is particularly suited to segment such structures from pointwise seeds (see Figure 5).

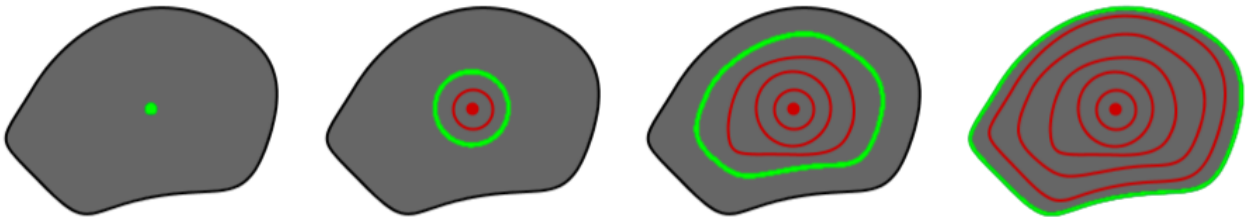

Figure 5. Evolution of a front propagation, starting from the initial center.

4.1 Segmentation by multiple fronts propagations

For each detected center (x_i), we propagate a front originating from x_i with a spatially varying speed $F(x)$ (detailed in Section 4.2). This can be done by solving the following eikonal equation

$$|\nabla T_i(x)|\ F(x) = 1 \qquad \text{with} \qquad T_i(x_i) = 0. \tag{10}$$

where $T_i(x)$ is the arrival time of the i-th front at point x. An efficient way to obtain the numerical solution is the Fast Marching method [9].

To avoid unwanted merging, each center generates its own front and we constrain the propagation so that two fronts cannot interpenetrate : a front cannot pass through a voxel which has already been visited by another front. This allows us to define for each detection a set of possible segmentations $\Omega_i(t) = \{x \mid T_i(x) \leq t\}$. The choice of the best threshold t_i^* is a common problem with front propagation methods. Here we choose t_i^* so that the generated segmentation Ω_i^* maximizes the gradient flux through its boundary :

$$\Omega_i^* = \Omega_i(t_i^*) \qquad \text{where} \qquad t_i^* = \underset{t>0}{\operatorname{argmax}} \left\{ \int_{\partial\Omega_i(t)} \left\langle \vec{\nabla} I(x), \vec{n}(x) \right\rangle dx \right\} \tag{11}$$

where $\vec{n}(x)$ is the normal to the domain boundary at point x. The choice of t_i^* is made independently for each front, which allows a robust segmentation of structures of different sizes. Note that using Stokes formula, the surface integral can be rewritten as a volume integral :

$$\int_{\partial\Omega_i(t)} \left\langle \vec{\nabla} I(x), \vec{n}(x) \right\rangle dx = \int_{\Omega_i(t)} \Delta I(x)\ dx \tag{12}$$

where Δ is the laplacian operator. Therefore, this criterion can be easily computed and accumulated during the front propagation.

4.2 Choice of the propagation speed

The function F represents the speed of the propagating front. It should therefore be high in areas that we consider to be inside the lesion. For our application, we choose

$$F(x) = \left(\frac{1}{\tilde{I}(x)^2 + \varepsilon^2} + \gamma \right) M_K(x) + \varepsilon \tag{13}$$

The first term in the brackets depends on the image intensity : lesions are anechoic so F should be a decreasing function of $\tilde{I}$. The second term is a regularization term, weighted by the parameter $\gamma > 0$. If γ goes to infinity, the propagation is isotropic and the fronts are spheres. If γ is zero, the propagation is driven only by the data-term, which yields better precision but a risk of leakage. In practice, γ is thus taken as a trade-off between regularity and precision. Finally, the multiplication by M_K (defined in Section 2.2) constrains the propagation inside the kidney: outside the mask, the propagation speed is null. The only purpose of the parameter ε is to avoid numerical instabilities. Figure 6 illustrates the propagation in a lesion with such a potential.

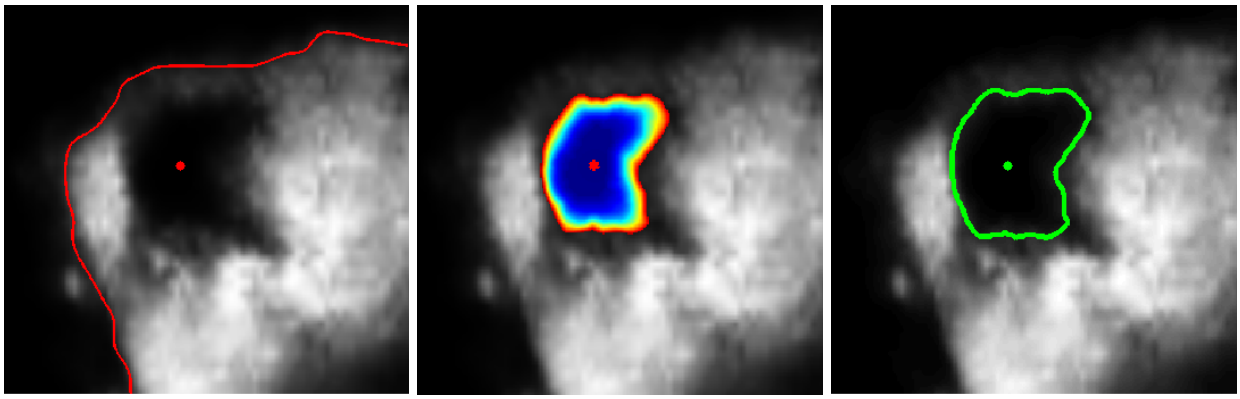

Figure 6. (a) Zoom on a 2D slice from Figure 1, with the detected center and the mask of the kidney (red). (b) Arrival time of the front generated from the center, with the speed F defined in Section 4.2. (c) Final segmentation of the lesion (green).

5. RESULTS AND DISCUSSION

Our algorithm was implemented in C++ on a standard computer (Intel Core i5 CPU @ 2.67 GHz with 4GB RAM). For a $256 \times 256 \times 256$ volume, the computational time was less than 150ms for the guided filtering,

around 500ms for each scale of the fast radial symmetry transform, and 1500ms for the fast marchig to recover the lesions segmentation. Therefore, the whole algorithm returns the results in around 5 seconds for a clinically relevant range of scales (e.g. $[5\text{ mm}, 20\text{ mm}]$).

We tested our method on synthetic images and 7 clinical acquisitions. Results on some of them are shown in Figures 7, 8, 9 and 10, and are discussed hereafter.

- Figures 7 and 8 depict cases where the kidney contains one single and large lesion. In both cases, the lesion is correctly detected and segmented, without any false detection. Even if the necrotic zones are not really spherical, the front propagation allows to segment them precisely.

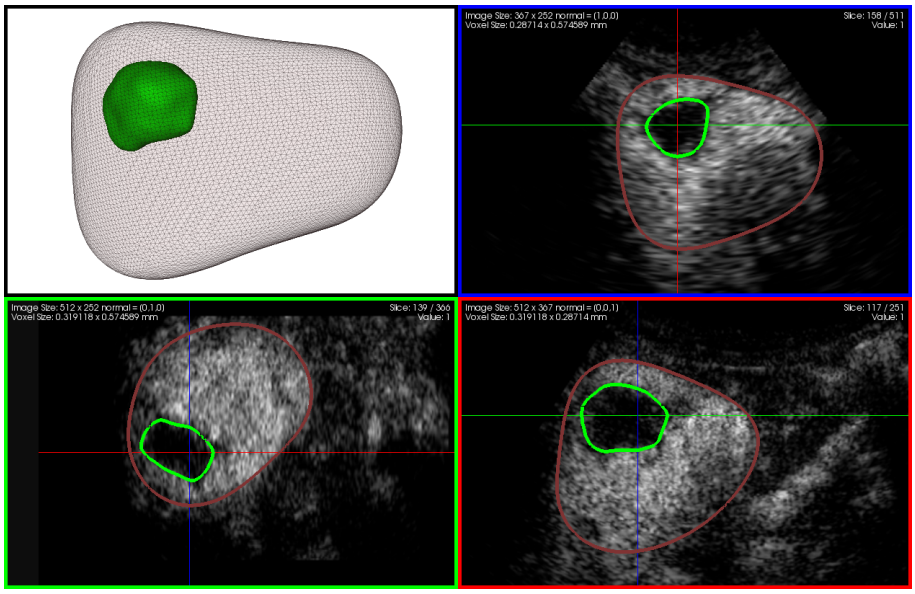

Figure 7. 3D visualization, and orthogonal slices of the segmentation results in green, with the kidney in red (single lesion).

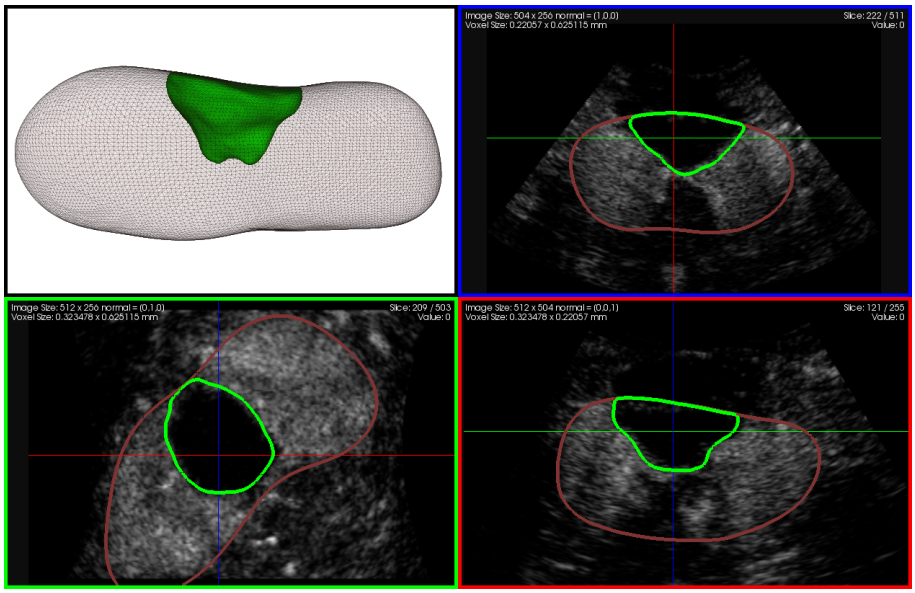

Figure 8. 3D visualization, and orthogonal slices of the segmentation results in green, with the kidney in red (single lesion).

- Figure 9 presents a more complicated case. The patient has a lot of cysts, and some dark tubular structures (which are not lesions) are visible. We show that our algorithm is able to extract almost all of the cysts, but is still specific: the tubular structures are not detected. Moreover, adjacent cysts (like the green and the pink or the yellow and the purple) are not merged, even if their separation is thin. This is due to the edge-preserving filtering on the ond hand, and on the other hand the constraint in our front propagation.

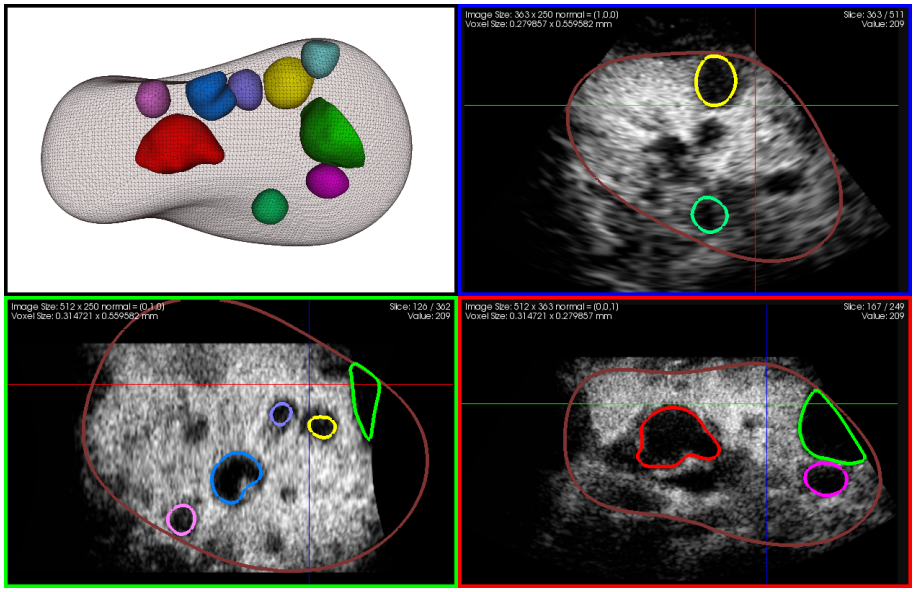

Figure 9. 3D visualization, and orthogonal slices of the segmentation results in various colors and the kidney in red (multi-lesions).

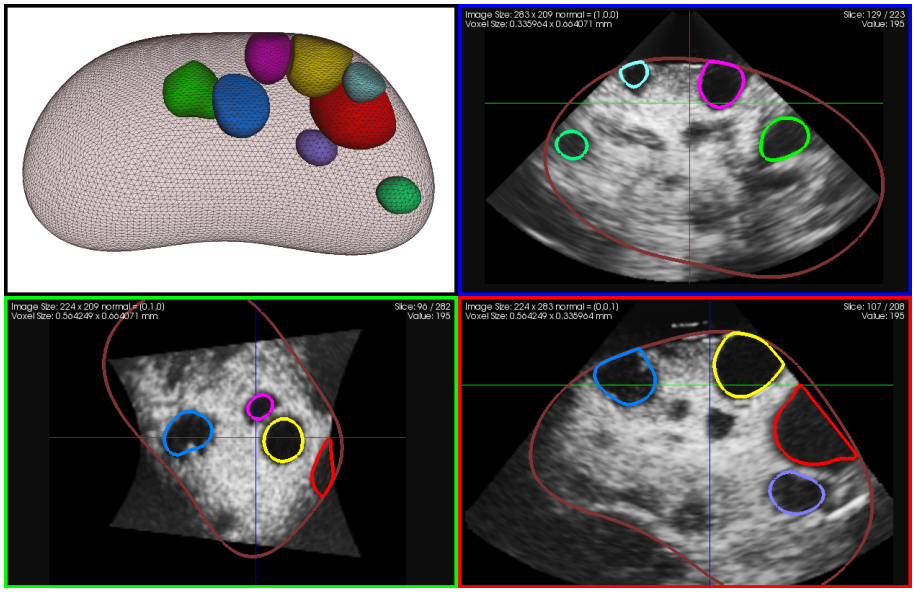

Figure 10. 3D visualization, and orthogonal slices of the segmentation results in various colors and the kidney in red (multi-lesions).

- The image shown in Figure 10 has been acquired from the same patient as the one in Figure 9, but with a lower resolution. Despite the poorer quality, the largest cysts are once again correctly detected and segmented.

Figure 11 compares the segmentation obtained from the last two images. The colors of the lesions were set manually so that two lesions of the same color correspond to each other (except those in gray). One may notice the similarity of the segmentation results, despite the difference of the two original images (ultrasound probe, resolution, field of view). Therefore, this comparison shows the potential of our method to register two CEUS volumes of the same patient, even if they are acquired in different conditions.

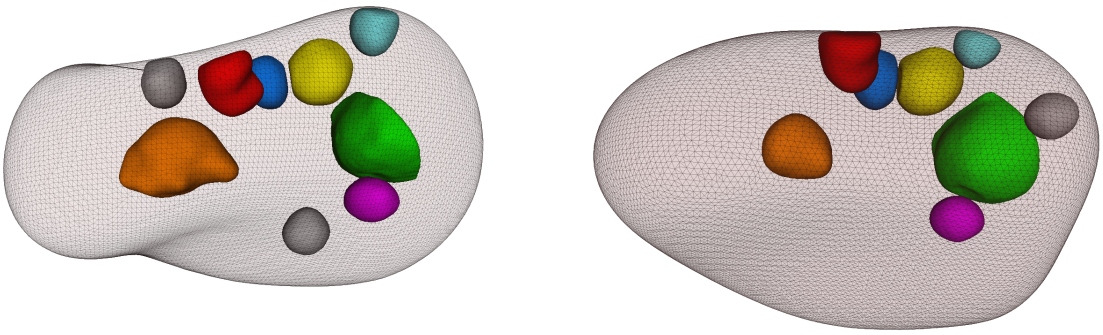

Figure 11. Segmentation of the kidney and the lesions from two different images of the same patient. Lesions of the same colors correspond to each other and lesions in gray have no correspondance (colors were set manually).

6. CONCLUSION

We presented a novel method to segment automatically cysts or necrotic volumes in 3D CEUS kidney images. Although the detection could be robustified, early results are very promising. To improve our algorithm, a shape analysis could be performed on each structure detected to discard those which are not big enough to be significant or whose shape differ too much from a sphere. We plan to validate our method quantitatively by comparing the results to a ground truth. Future work also include the use of the segmented structures as features in the registration of CEUS to CEUS (or CEUS to CT/MR) images.

REFERENCES

[1] Albrecht, T., Blomley, M., Bolondi, L., Claudon, M., Correas, J., Cosgrove, D., Leen, E., Lencioni, R., Lindsell, D., Martegani, A., et al., "Guidelines for the use of contrast agents in ultrasound," *Ultraschall Med* **25**(4), 249–256 (2004).

[2] Meloni, M., Bertolotto, M., Alberzoni, C., Lazzaroni, S., Filice, C., Livraghi, T., and Ferraioli, G., "Follow-up after percutaneous radiofrequency ablation of renal cell carcinoma: contrast-enhanced sonography versus contrast-enhanced CT or MRI," *American Journal of Roentgenology* **191**(4), 1233–1238 (2008).

[3] Gasnier, A., Ardon, R., Ciofolo-Veit, C., Leen, E., and Correas, J. M., "Assessing tumour vascularity with 3D contrast-enhanced ultrasound: a new semi-automated segmentation framework," in [*Proceedings of the 2010 IEEE international conference on Biomedical imaging: from nano to Macro*], *ISBI'10*, 300–303, IEEE Press, Piscataway, NJ, USA (2010).

[4] Kissi, A., Cormier, S., Pourcelot, L., Bleuzen, A., and Tranquart, F., "Contrast enhanced ultrasound image segmentation based on fuzzy competitive clustering and anisotropic diffusion," in [*International Conference of the IEEE Engineering in Medicine and Biology Society*], IEEE, San Francisco, USA (Sept. 2004).

[5] He, K., Sun, J., and Tang, X., "Guided image filtering," in [*Computer Vision – ECCV 2010*], Daniilidis, K., Maragos, P., and Paragios, N., eds., *Lecture Notes in Computer Science* **6311**, 1–14, Springer (2010).

[6] Loy, G. and Zelinsky, A., "Fast radial symmetry for detecting points of interest," *IEEE Trans. Pattern Anal. Mach. Intell.* **25**, 959–973 (August 2003).

[7] Duda, R. O. and Hart, P. E., "Use of the Hough transformation to detect lines and curves in pictures," *Commun. ACM* **15**, 11–15 (Jan. 1972).

[8] Lindeberg, T., "Feature detection with automatic scale selection," *International Journal of Computer Vision* **30**, 79–116 (1998).

[9] Malladi, R. and Sethian, J. A., "A real-time algorithm for medical shape recovery," in [*Proceedings of the Sixth ICCV*], *ICCV '98*, 304–, IEEE Computer Society, Washington, DC, USA (1998).